INTERNATIONAL JOURNAL FOR NUMERICAL METHODS IN FLUIDS
Int. J. Numer. Meth. Fluids 2005; **47**:423–447
Published online 14 December 2004 in Wiley InterScience (www.interscience.wiley.com). DOI: 10.1002/fld.812

Numerical predictions of low Reynolds number flows over two tandem circular cylinders

B. Sharman[1], F. S. Lien[2,*,†], L. Davidson[3] and C. Norberg[4]

[1] *Martec Limited, 1888 Brunswick Street, Suite 400, Halifax, Nova Scotia, Canada B3J 3J8*
[2] *Department of Mechanical Engineering, University of Waterloo, University Avenue West, Waterloo, Ont., Canada N2L 3G1*
[3] *Department of Thermo and Fluid Dynamics, Chalmers University of Technology, SE-412 96 Göteborg, Sweden*
[4] *Department of Heat and Power Engineering, Lund Institute of Technology, P.O. Box 118, SE-221 00, Lund, Sweden*

SUMMARY

Flows over two tandem cylinders were analysed using the newly developed collocated unstructured computational fluid dynamics (CUCFD) code, which is capable of handling complex geometries. A Reynolds number of 100, based on cylinder diameter, was used to ensure that the flow remained laminar. The validity of the code was tested through comparisons with benchmark solutions for flow in a lid-driven cavity and flow around a single cylinder. For the tandem cylinder flow, also mesh convergence was demonstrated, to within a couple of percent for the RMS lift coefficient.

The mean and fluctuating lift and drag coefficients were recorded for centre-to-centre cylinder spacings between 2 and 10 diameters. A critical cylinder spacing was found between 3.75 and 4 diameters. The fluctuating forces jumped appreciably at the critical spacing. It was found that there exists only one reattachment and one separation point on the downstream cylinder for spacings greater than the critical spacing.

The mean and the fluctuating surface pressure distributions were compared as a function of the cylinder spacing. The mean and the fluctuating pressures were significantly different between the upstream and the downstream cylinders. These pressures also differed with the cylinder spacing. Copyright © 2004 John Wiley & Sons, Ltd.

KEY WORDS: two tandem circular cylinder; unsteady flows; unstructured grid

1. INTRODUCTION

The interaction of the flow over multiple bodies is becoming an increasingly popular field of research. Such structures abound in engineering. Examples include groupings of electrical

*Correspondence to: F. S. Lien, Department of Mechanical Engineering, University of Waterloo, University Avenue West, Waterloo, Ont., Canada N2L 3G1.
†E-mail: fslien@uwaterloo.ca

Contract/grant sponsor: NSERC

Received 2 April 2003
Revised 4 October 2004
Accepted 15 October 2004

transmission lines, bundles of tubes in heat exchangers, bridge piers and cables, skyscrapers in a city and the pipes from an oil platform to the bottom of the ocean.

Cylindrical geometries often appear in engineering structures. Although these structures are very simple, the fluid flow around them is not. The circular cylinder is a bluff body and forms a large separated wake. Separated wakes are nearly impossible to predict analytically and hence must be found either through experimentation or numerical simulation. Unlike rectangular cylinders, where the flow separates from the corners, the flow can separate from any location on a circular cylinder, further complicating analyses.

The difficulty in predicting flow around circular cylinders is multiplied when two or more of these cylinders are placed in proximity to each other. The large separated wakes from each of the cylinders interact with each other to form a flow that is greatly different than the flow around a single cylinder. The exact form of the interaction is highly dependent on the Reynolds number of the flow and on the cylinder placement.

There is an infinite number of ways to place cylinders in proximity to one another. The fluid velocity can also be varied. In order to reduce the number of simulations, only combinations where one cylinder lies directly behind the other, tandem arrangement, were considered. Simulations were conducted for a single flow velocity, corresponding to a Reynolds number of 100 when based on the cylinder diameter. This flow is laminar.

The study of flow over two cylinders has a much shorter history than that of flow over a single cylinder. While a few studies were conducted beforehand, interest in flow over multiple cylinders picked up in the mid 1970s and has continued to date. Most of the studies were experimental investigations, although a handful of numerical simulations have recently been conducted.

In 1977, Zdravkovich [1] summarized a variety of measurements of drag forces on two circular cylinders in tandem arrangement. Ohya *et al.* [2] updated Zdravkovich's compilation in 1989. These authors considered Reynolds numbers between 80 and 2.3×10^5 and cylinder spacings of up to 30 diameters. They found that the drag force is largely dependent on the Reynolds number and the cylinder spacing. A sudden increase in the drag coefficient of both the upstream and the downstream cylinders occurs at the *critical spacing*, s_c, where the symbol s refers to the non-dimensionalized cylinder spacing. For all but low Reynolds numbers with laminar shedding, s_c is around 3.6.

Igarashi [3] conducted a detailed examination of the flow structure around two tandem cylinders for Reynolds numbers between 3300 and 60 000. Following Zdravkovich [4] and valid for his compilation at Reynolds numbers within the upper subcritical regime for the single cylinder ($Re = 5000$–$300\,000$ approximately), the tandem cylinder flow changes with relative cylinder spacing as follows (limits and appearance of flow patterns are dependent on the Reynolds number, see also Reference [5]):

$s < 1.1$: the two cylinders act as a single object. The fluid between the two cylinders is stagnant. The flow does not reattach to the downstream cylinder.

$1.1 < s < 1.6$: the flow alternately reattaches to one side and then the other side of the downstream cylinder. A vortex street still only exists behind the rear cylinder.

$1.6 < s < 2.4$: both sides of the wake from the upstream cylinder are attached to the downstream cylinder.

$2.4 < s < 3.4$: the occasional reattachment onto the rear cylinder is disrupted. Consistent vortices are not shed off the front cylinder.

$3.4 < s < 3.8$: some of the vortices roll up before striking the rear cylinder, but others do not. This is called bistable flow.

$s > 3.8$: vortices shed off the front cylinder roll up before striking the rear cylinder. A vortex street is formed behind both cylinders. The vortices shed off the front cylinder interact strongly with the vortices shed off the rear cylinder, causing the vortices shed off the rear cylinder to become extremely powerful.

Flow over a single cylinder is known to transition to turbulence for Reynolds numbers between 180 and 200 [1]. Flow visualizations of Huhe-Aode *et al.* [6] and Tanida *et al.* [7] show that the flow for $Re = 100$ is laminar for all cylinder spacings. For $Re = 300$, they report the formation of a turbulent vortex street when the cylinder spacing is greater than the critical cylinder spacing. Their results also show the presence of a critical spacing for low Reynolds number flows. They report a large Reynolds number dependence of the Strouhal number and of the critical spacing. The critical spacing drops from $4.5 \leqslant s_c \leqslant 5$ for $Re = 100$ to $3.5 \leqslant s_c \leqslant 4$ for $Re = 300$ and finally to $3 \leqslant s_c \leqslant 3.5$ for $Re = 1000$.

One interesting observation of the results for Huhe-Aode *et al.* is that for $Re = 100$, the Strouhal number stays constant at 0.14 as the cylinder spacing is increased from $s = 5$ to 10. Instead, it is expected that the Strouhal number would approach that of a single cylinder, 0.164, as the spacing is increased. In their experiments, Huhe-Aode *et al.* used a 30 cm long cylinder with a diameter of 1 cm cantilevered from one of the walls. A 10 cm gap existed between the end of the cylinder and the other wall. No end plates were used.

Measurements by Norberg [8] and Williamson [9] show the Strouhal number for flow over a single cylinder as the aspect ratio, AR, is increased. They showed that the Strouhal number is around 0.14 for aspect ratios of 30 and below and around 0.16 for higher aspect ratios. The results of Norberg and Williamson confirm that Huhe-Aode *et al.* conducted their tests using cylinders of insufficient aspect ratio, hence their results are not representative of flow over two infinitely long circular cylinders in tandem arrangement.

Numerical studies have been conducted for a Reynolds number of 100 by Li *et al.* [10] and Mittal *et al.* [11], and for a Reynolds number of 200 by Slaouti and Stansby [12] and by Meneghini *et al.* [13]. The results of current simulations have been compared against those of Li *et al.* in spite of the fact that limited computer power forced them to use a coarse mesh. Results were not compared against those of Mittal *et al.* as they only presented data for two cylinder spacings, which makes it difficult to compare trends. Also, the results were not compared against those of Slaouti and Stansby and Meneghini *et al.* due to the different Reynolds number.

2. NUMERICAL METHOD

Unstructured meshes are used because meshing complicated domains is easy using freely available meshing packages, such as MESH2D [14] and EasyMesh [15]. A more involved discretization of the continuity and the Navier–Stokes equations is required for unstructured meshes than for structured meshes. This section highlights the numerical discretization method used in the collocated unstructured computational fluid dynamics (CUCFD) code, which was used for all of the analyses presented in this paper.

Equations (1) and (2) show the integral form of the incompressible continuity and the Navier–Stokes equations, respectively. A non-moving control volume is assumed.

$$\int_S \rho(\mathbf{v}\cdot\hat{\mathbf{n}})\,\mathrm{d}S = 0 \tag{1}$$

$$\frac{\partial}{\partial t}\int_\Omega \rho v_i\,\mathrm{d}\Omega + \int_S \rho v_i(\mathbf{v}\cdot\hat{\mathbf{n}})\,\mathrm{d}S = \int_S T_{ij}\cdot\hat{\mathbf{n}}\,\mathrm{d}S \tag{2}$$

$$T_{ij} = -p\delta_{ij} + \mu\left(\frac{\partial v_i}{\partial x_j} + \frac{\partial v_j}{\partial x_i}\right)$$

Equations (1) and (2) are non-dimensionalized by the following dimensionless groups:

$$\bar{x} = \frac{x}{L_{\mathrm{ref}}}, \quad \bar{y} = \frac{y}{L_{\mathrm{ref}}}, \quad \bar{u} = \frac{u}{U_{\mathrm{ref}}}, \quad \bar{v} = \frac{v}{U_{\mathrm{ref}}}, \quad \bar{p} = \frac{p}{\rho U_{\mathrm{ref}}^2} \tag{3}$$

Substituting Equation (3) in Equation (2) gives us the dimensionless stress tensor $\bar{T}_{ij}$:

$$\bar{T}_{ij} = -\bar{p}\delta_{ij} + \frac{1}{Re}\left(\frac{\partial \bar{v}_i}{\partial \bar{x}_j} + \frac{\partial \bar{v}_j}{\partial \bar{x}_i}\right)$$

where Re is the Reynolds number, defined as $Re = \rho U_{\mathrm{ref}} L_{\mathrm{ref}}/\mu$. L_{ref} and U_{ref} in Equation (3) are the reference length and the velocity, respectively. For example, for flow over a circular cylinder of diameter D in a free stream at a speed of U_∞, $L_{\mathrm{ref}} = D$ and $U_{\mathrm{ref}} = U_\infty$. The overbar signs are dropped for convenience in Sections 3–5 where all variables mentioned are in dimensionless form.

A cell-centred unstructured mesh divides the domain into triangular control volumes, or cells. Figure 1 shows a control volume P and its immediate neighbours. The flow variables, velocity and pressure, are stored using a collocated variable arrangement, which means that all of these values are stored at the cell centroids. Rhie–Chow interpolation [16] is used to stop pressure checkerboarding from occurring.

Two notations are used in this work, one for calculations being conducted on a cell and the second is used for calculations being conducted on a face. Figure 1 shows a cell and its neighbours, which are referenced when using cell-based calculations. Normally the term nb

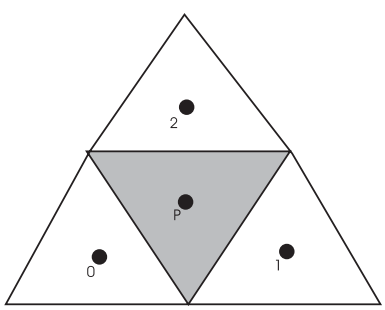

Figure 1. Cell-centred control volume.

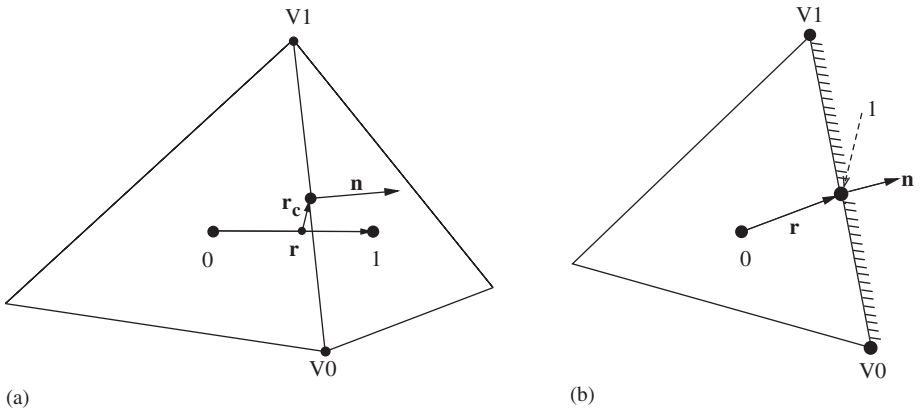

Figure 2. Geometry for face-based discretization: (a) Interior face, and (b) Boundary face.

is used in this work to refer to a neighbour of cell P instead of referring to the neighbouring cells individually.

Figure 2 shows the notation that is used for face-based calculations. The vertices $V0$ and $V1$ are always counter-clockwise for cell 0 and clockwise for cell 1. The face normal is defined as pointing outwards from cell 0.

For boundaries, cell 1 is always the boundary cell and cell 0 is always the interior cell. A boundary cell has no volume, hence the face midpoint occurs at the exact same spot as the centroid. The normal of a boundary face always points out of the domain, as it points outwards from cell 0.

The momentum and the pressure-correction equations were solved iteratively using the SIMPLE algorithm [17].

2.1. Gradients

According to the Green–Gauss theorem [18]:

$$\frac{\partial \phi}{\partial x} = \frac{1}{\Omega} \oint \phi \, \mathrm{d}y, \quad \frac{\partial \phi}{\partial y} = -\frac{1}{\Omega} \oint \phi \, \mathrm{d}x \tag{4}$$

When using a finite-volume approach, ϕ is assumed to be constant within a control volume and constant along each face. Hence Equation (4) can be simplified to Equation (5). Here, $\phi_f = 0.5(\phi_P + \phi_{\mathrm{nb}})$ for internal cells and $\phi_f = \phi_{\mathrm{bnd}}$ for boundary cells. $\Delta x_f = x_{V1} - x_{V0}$ and $\Delta y_f = y_{V1} - y_{V0}$ for neighbour 0 of the face while $\Delta x_f = x_{V0} - x_{V1}$ and $\Delta y_f = y_{V0} - y_{V1}$ for neighbour 1 of the face.

$$\frac{\partial \phi}{\partial x} = \frac{1}{\Omega} \sum_{\mathrm{nb}} \phi_f \Delta y_f, \quad \frac{\partial \phi}{\partial y} = -\frac{1}{\Omega} \sum_{\mathrm{nb}} \phi_f \Delta x_f \tag{5}$$

Zwart [19] found that under-relaxing the gradients during the solution iteration significantly improved the convergence rate. This was verified in the present study. The gradients are

relaxed as follows:

$$\nabla\phi_P = \alpha_{\text{grad}}\nabla\phi_{P,\text{new}} + (1-\alpha_{\text{grad}})\nabla\phi_{P,\text{old}} \tag{6}$$

$\alpha_{\text{grad}} \approx 0.8$ is the recommended gradient under-relaxation parameter.

2.2. Discretization of the momentum equations for steady-state flows

Equation (7) is the general form of the linearized momentum equation for the conservation of the ith component of momentum. The A_P, A_{nb} coefficients and the source term, B_i, must be calculated for every cell. The equations for the coefficients and the cells have been fully presented in Reference [20]. They can be derived from the discretizations shown in this work.

$$A_P v_{i,P} = \sum_{\text{nb}} A_{\text{nb}} v_{i,\text{nb}} + B_i \tag{7}$$

2.2.1. Discretization of the advection terms. The advection of the ith component of momentum can be written for a control volume as

$$\sum_f m_f v_{i,f} \tag{8}$$

where m_f is the mass flux into or out of the control volume. The mass flux is calculated as part of the pressure-correction equation, see Section 2.3, and is stored for use in Equation (8).

The discretization scheme for $v_{i,f}$ of Zwart [19] is modified slightly to improve upon the accuracy of his discretization.

$$\begin{aligned} v_{i,f} &= v_{i,0} + (\nabla v_i)_0 \cdot \mathbf{r}_{0-f}, \quad m_f > 0 \\ v_{i,f} &= v_{i,1} + (\nabla v_i)_1 \cdot \mathbf{r}_{1-f}, \quad m_f < 0 \end{aligned} \tag{9}$$

The face midpoint is not necessarily at the same point as the midpoint between cell centroids 0 and 1. Hence the $\mathbf{r}_{0-f}$ or the $\mathbf{r}_{1-f}$ vector is the vector from the centroid of cell 0 or 1, respectively, to the face midpoint and not simply half of the vector between the centroids of cells 0 and 1.

2.2.2. Discretization of the viscous terms. The viscous force on a face can be written as

$$F_{i,v} = -\mu(\nabla v_i \cdot \hat{\mathbf{n}}_f)S_f \tag{10}$$

Discretization proceeds by decomposing $F_{i,v}$ as shown in Equation (11). Advantages of this scheme are that it is linearly exact and that it requires no modification between two-dimensional and three-dimensional flows.

$$F_{i,v} = -\mu(\nabla v_i \cdot (\alpha\hat{\mathbf{r}}) + \overline{\nabla v_i} \cdot (\hat{\mathbf{n}}_f - \alpha\hat{\mathbf{r}}))S_f \tag{11}$$

where

$$\nabla v_i \cdot (\alpha\hat{\mathbf{r}}) = \alpha\frac{v_{i,1} - v_{i,0}}{|\mathbf{r}|} \tag{12}$$

α is a scaling factor. Zwart recommends using $\alpha = \hat{\mathbf{n}}_f \cdot \hat{\mathbf{r}}$. This ensures that the $\overline{\nabla v_i} \cdot (\hat{\mathbf{n}}_f - \alpha\hat{\mathbf{r}})$ term is used only for non-orthogonal contributions to $F_{i,v}$.

2.2.3. Discretization of the pressure terms. The pressure force on one face of a control volume can be written as

$$F_{p,i} = p_f \hat{n}_{f,i} S_f \tag{13}$$

For unstructured grids, the face midpoint may be different from the midpoint of the cell-centroids, hence a correction is required to transfer the pressure from the midpoint of the two cell centroids to the face midpoint.

$$p_f = \frac{1}{2}(p_0 + p_1) + \overline{\nabla p} \cdot \mathbf{r}_c \tag{14}$$

2.2.4. Discretization of transient terms. The Crank–Nicolson method was used to discretize the following transient term:

$$\frac{\partial}{\partial t} \int_V \rho v_i \, \mathrm{d}\Omega \tag{15}$$

A description of this method can be found in Reference [21]. This method is of second-order accuracy.

2.3. Discretization of the pressure-correction equation for steady-state flows

The pressure-correction equation is used to adjust the pressure so that the continuity equation is satisfied. The discretized form of the pressure-correction equation is

$$a_P p'_P = \sum a_{\mathrm{nb}} p'_{\mathrm{nb}} - R_m \tag{16}$$

R_m is the mass imbalance, which is defined as $R_m = \sum_{\mathrm{nb}} m_f$.

The a_{nb} coefficients were obtained from sample codes provided by Ferziger and Peric [21]. They are presented here without derivation. The A_P coefficient is that of the discretized momentum equation. The a_{nb} coefficient is the same for both cells of a face. The a_{nb} coefficients are calculated using face-based looping.

$$a_{\mathrm{nb}} = \frac{1}{2} \rho S_f^2 \left(\frac{1}{(A_P)_0} + \frac{1}{(A_P)_1} \right) \tag{17}$$

The a_P coefficient is the sum of the a_{nb} coefficients in the cell.

Following the Rhie–Chow interpolation [16], the mass flow through a face is given by

$$m_f = \rho(\hat{\mathbf{n}}_f \cdot \mathbf{v}_{\mathrm{avg}}) S_f - a_{\mathrm{nb}}(p_1 - p_0 - \overline{\nabla p} \cdot \mathbf{r}) \tag{18}$$

where

$$v_{i,\text{avg}} = \frac{1}{2}(v_{i,0} + v_{i,1}) + \overline{\nabla v_i} \cdot \mathbf{r}_\mathbf{c} \tag{19}$$

The pressure-correction equation is solved using a Jacobian preconditioned conjugate gradient solver [22]. The pressure-corrections are used to update the cell pressures, Equation (20), and the face mass fluxes, Equation (21).

$$p = p^* + \alpha_P p' \tag{20}$$

$$m_f = m_f^* + a_{\text{nb}}(p'_0 - p'_1) \tag{21}$$

α_p is the under-relaxation factor for p'. This is required as the SIMPLE algorithm over-predicts the pressure corrections [21]. There is no set under-relaxation parameter, but α_p is usually quite low, in the vicinity of 0.1–0.3. A rule of thumb is that the under-relaxation parameters for the momentum equations and the pressure-correction equation should sum to 1.

Corrections to the face velocities are made using Equation (22). While the face velocities are not stored, the cell-centroid velocity is corrected by the average of the face velocity corrections.

$$v'_{f,i} = -\hat{n}_{f,i}(p'_1 - p'_0)\frac{1}{2}\left(\frac{1}{A_{P,0}} + \frac{1}{A_{P,1}}\right)S_f \tag{22}$$

2.4. Boundary faces

The effects of boundaries are treated in the bordering interior cells. After the velocities and pressure corrections for the interior cells are calculated, the boundary values are extrapolated from the interior of the domain for Neumann boundary conditions, or they are specified for Dirichlet boundary conditions.

After the pressure is corrected, the boundary-cell pressure is extrapolated from its interior neighbour using $p_1 = p_0 + \nabla p_0 \cdot \mathbf{r}_{0-1}$. A zero-flux Neumann boundary condition is always used for the pressure-correction equation.

Outlet boundaries: A convective boundary condition is used for transient flows, and is specified in the following equation:

$$\frac{\partial v_i}{\partial t} + U_{\text{bulk}}\frac{\partial v_i}{\partial n} = 0 \tag{23}$$

In Equation (23), U_{bulk} is called the bulk velocity. It is taken as being the average inlet velocity. The same bulk velocity is used when extrapolating all velocity components to the outlet boundary. Le and Moin [23] reported that the convective boundary condition allowed vortical structures to exit the outer boundary, even with a short domain, with very little distortion.

Equation (23) is not applied directly to the boundary-cell centroid, but instead to a different point on the outlet boundary, called the OP point in Figure 3. The OP point is placed so that the normal vector of the boundary passing through the OP point touches the interior cell centroid.

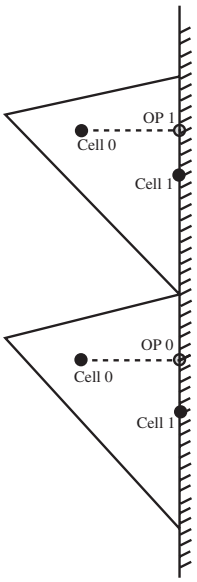

Figure 3. Extrapolation to outlet boundaries.

The velocities at boundary-cell centroids are calculated by a linear interpolation between the surrounding OP points. The pressure at the boundary cell is taken as being the same as that of its interior neighbour.

3. LID-DRIVEN CAVITY

Test cases against benchmark solutions were conducted to verify the accuracy of the discretization scheme and to test for programming errors. The lid-driven cavity test case is a good and simple first test case. It is simple in that it is easy to obtain a converged solution. It is also difficult to obtain accurate solutions, especially for higher Reynolds numbers. Hence this test gives an indication of the accuracy of the discretization of the momentum and the continuity equations. The results were compared against benchmark solutions provided by Emvin [24], who used a third-order finite-element scheme on an extremely fine unstructured mesh.

The lid-driven cavity is a square box where the top wall slides to the right at a constant speed. The other three walls are stationary. Two different meshes were used for the benchmark testing. Figure 4 shows the domain and the 8534 cell mesh, which is the finer of the two meshes.

Tests were conducted for an intermediate Reynolds number of 1000, where the Reynolds number is based on the length of the square box and the speed of the top wall. Figure 5 shows flow streamlines. Profiles of the u-velocity along the line $x = 0.5$ and the v-velocity along the line $y = 0.5$ were compared against benchmark solutions in Figures 6(a) and 6(b), respectively. The velocity profiles were found to agree very closely with the benchmark solution.

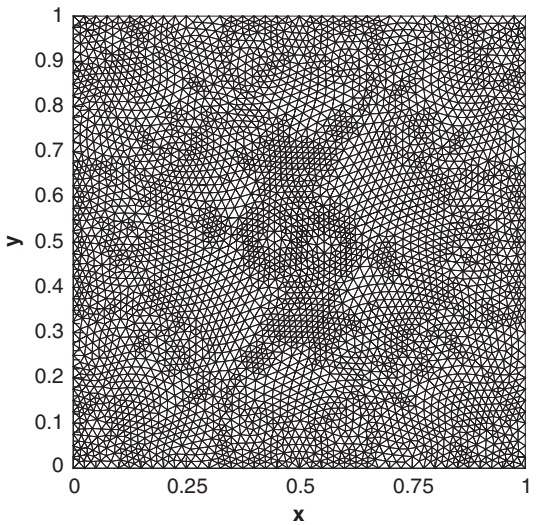

Figure 4. The computational mesh containing 8534 cells for the lid-driven cavity test case.

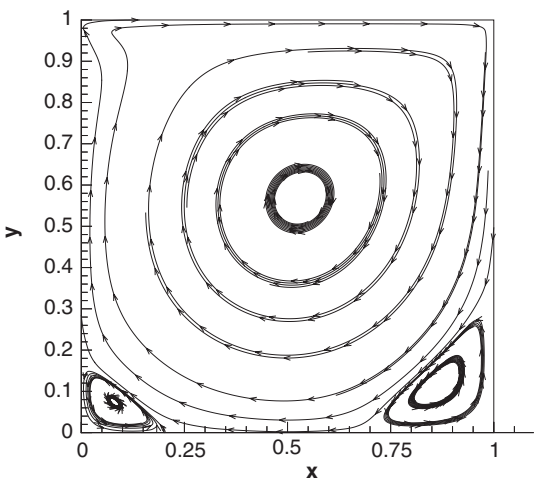

Figure 5. Streamlines in the lid-driven cavity, $Re = 1000$.

4. SINGLE CIRCULAR CYLINDER

Before simulating the flow over two circular cylinders in tandem arrangement, it is useful to first simulate the flow around a single circular cylinder. Not only is this good to test the accuracy of the CUCFD program, as good quality benchmarks are available, but it also serves as a reference to judge the effects of adding the second cylinder.

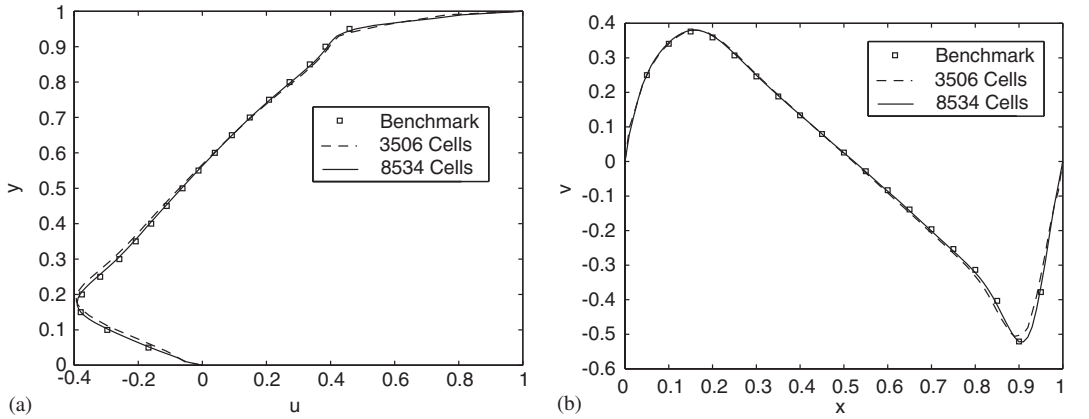

Figure 6. u-velocity profiles at $x = 0.5$, (a), and v-velocity profiles at $y = 0.5$, (b), for $Re = 1000$.

Numerical simulations have been conducted since the early 1970s on flow over circular cylinders. Norberg [25] has compiled an extensive list comparing the RMS lift coefficient, C_l', for over 60 numerical simulations. Examining this list, the spread in the predictions for C_l' becomes apparent. This spread gives an indication of the complexity of the flow and its sensitivity to the domain size and to the mesh. Recently, numerical results have converged upon results that are now accepted.

The Reynolds number has a large effect on the flow around a circular cylinder. It is defined as $Re = \rho U_\infty D/\mu$, where ρ is the fluid density, U_∞ is the free-stream fluid velocity, D is the diameter of the cylinder and μ is the dynamic viscosity. At a Reynolds number of 100, the flow is laminar and the wake fluctuates periodically.

4.1. Domain and mesh

The inlet was placed 12.5 diameters upstream of the cylinder. Slip boundaries, $\mathrm{d}u/\mathrm{d}y = 0$ and $v = 0$, were placed 25 diameters above and below the cylinder. This gave a blockage ratio, the ratio between the cylinder diameter and the height of the channel, of 2%. The outlet was placed 25 diameters downstream of the cylinder to reduce errors propagating into the solution.

Simulations were run with a mesh of 8320 cells and with a mesh of 14 441 cells, only results from the 14 441 cell mesh are shown. For this mesh (see Figure 7), a three-diameter mesh seed was used along the upper and lower slip boundaries and along inlet and outlet boundaries away from the centre. Within 10 diameters above and below the centre-line, the mesh seeding on the inlet was refined to one diameter and the mesh seeding on the outlet was refined to 0.5 diameters. A refinement box of mesh seeding 0.5 diameters had lower left and upper right corners of $(-10, -10)$ and of $(23, 10)$ diameters, respectively, in order to capture any effects near the cylinder and the fluctuations in the cylinder wake. The mesh spacing close to the cylinder surface is $\pi/90 = 0.0349$.

4.2. Results

This flow is not steady-state. Instead the free-shear layers in the wake roll up, causing vortices to be shed alternately from the top and the bottom of the cylinder. The simulations were able

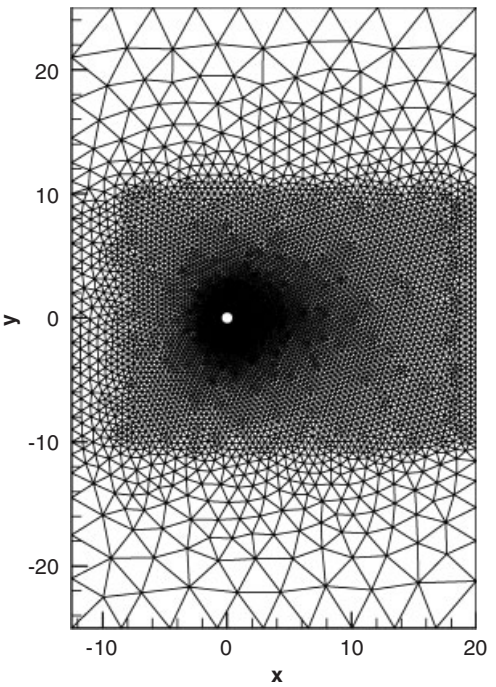

Figure 7. The computational mesh containing 14 441 cells for flow over a single circular cylinder at $Re = 100$.

to capture the vortex shedding phenomenon without the need of having to trigger it through artificial instabilities. Conceivably, vortex shedding was triggered by small differences between the top and bottom of the flow caused by the non-symmetrical unstructured mesh.

The shedding frequency is presented as the non-dimensional Strouhal number, $St = f_s D/U_\infty$, where f_s is the shedding frequency, D is the diameter of the cylinder while U_∞ is the free-stream velocity.

The vortices shed from the cylinder cause the lift and drag forces to fluctuate. These forces can be represented by a mean value and a fluctuating value. The fluctuating lift and drag components are presented using RMS (root-mean-square) values, $C_{\mathrm{RMS}} = \sqrt{\sum_{i=1}^{N} (C_i - C_{\mathrm{mean}})^2/N}$. Here, C_{RMS} (also referred to as C') is the RMS coefficient for either lift or drag, C_i is the lift or the drag coefficient at a single point in time, C_{mean} is the mean lift or drag coefficient while N is the number of samples used to calculate the RMS coefficient.

Mean and RMS coefficients were found by taking one sample for each timestep for exactly one vortex shedding cycle. Table I compares the solutions obtained from the 14 441 cell mesh against reliable numerical simulations. In this table, coefficients ending with a′ refer to RMS values while the others refer to mean values.

All fluctuating quantities from Posdziech and Grundmann and by Park *et al.* were given by the amplitude of the peak coefficients. Meanwhile the fluctuating quantities presented from the current work are presented using RMS values. In order to compare the different results, it

Table I. Comparison of obtained results vs. benchmark solutions for flow over a single circular cylinder, $Re = 100$.

	Posdziech and Grundmann	Park *et al.*	Current work
Year	2000	1998	—
Reference	[26]	[27]	—
Blockage ratio	0.0071	0.01	0.02
Number of cells/10^3	19	39	14
Strouhal number	0.164	0.165	0.164
C_d	1.32	1.33	1.33
C_{dv}	0.34	0.34	0.34
C_{dp}	0.99	0.99	0.99
C_{ps}	—	1.03	1.04
$-C_{pb}$	0.71	0.74	0.72
C_l'	0.23	0.23	0.23
C_{lv}'	0.031	0.030	0.030
C_{lp}'	0.20	0.21	0.20
C_d'	0.0063	0.0064	0.0064
C_{dv}'	0.0007	0.0007	0.0004
C_{dp}'	0.0058	0.0058	0.0058
C_l'/C_d'	36	36	35

For the data of Posdziech and Grundmann, the Strouhal number, C_d, C_l', C_{lv}', C_{lp}' and $-C_{pb}$ were given in Reference [26], the other results were provided by Posdziech.

is assumed that all of the forces fluctuate as sine waves. This assumption was proven to be very accurate. The RMS value of a sine wave is $1/\sqrt{2}$ times the amplitude of the wave. The fluctuating coefficients presented by Posdziech and Grundmann and by Park *et al.* shown in Table I have all been divided by the $\sqrt{2}$ factor.

Table I shows that excellent agreement was obtained for the shedding frequency and the lift and drag coefficients against recent numerical simulations for this test case. It also appears that decreasing the blockage ratio down from 0.02 has little effect.

A mean lift coefficient of 0.006 was calculated. This coefficient should be zero. This value gives an indication of the mesh dependence and the accuracy of the results as it is caused by the non-symmetrical unstructured mesh. The mean lift coefficient is 2.6% of the fluctuating RMS lift coefficient.

The surface pressure distribution on the cylinder surface was also recorded. The mean surface pressures and the RMS surface pressures are shown in Figures 8(a) and 8(b), respectively. The mean surface pressure distribution is compared against results reported by Park *et al.* The authors are unaware of any publication showing the RMS surface pressure distribution for laminar flows.

The mean surface pressure agrees very well with results of Park *et al.* [27]. The separation point was found by examining flow animations for locations on the surface where the vorticity is zero. It was found to vary between 118 and 122°.

The RMS pressure fluctuates greatly on the sides of the cylinder, but scarcely on the front and the rear, which explains why C_l' is so much larger than C_d'. For turbulent flows, a local

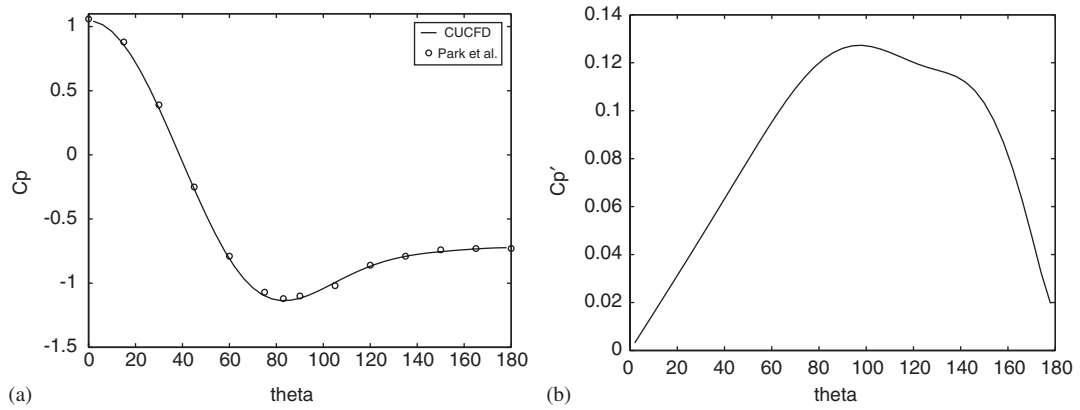

Figure 8. Mean (a), and RMS (b), surface pressure distributions for flow over a single cylinder, $Re = 100$.

maximum of the RMS pressure coefficient occurs near the location of flow separation. These results indicate that this is not the case for low Reynolds number flows.

5. TWO CIRCULAR CYLINDERS IN TANDEM ARRANGEMENT

Figure 9 shows the notation for the study of flow over two tandem cylinders. All simulations were conducted at a Reynolds number of 100. Flow over a single cylinder is laminar at $Re = 100$ [1]. According to Huhe-Aode *et al.* [6], this is also the case for flow over two tandem cylinders.

From an engineering standpoint, the lift and drag coefficients and the Strouhal numbers are crucial. They show the magnitude and the direction of the forces acting on the cylinders, and if these forces fluctuate near structural resonating frequencies. They offer, however, no clue to the fluid flow. Flow visualizations and surface pressure distributions are used to show the flow field and to explain the forces and the shedding frequencies.

5.1. Domain and mesh

The domain is very similar to that used for flow over a single circular cylinder at $Re = 100$, see Figure 10. The inlet was placed 12.5 diameters upstream of cylinder 1. The outlet was placed 20 diameters downstream of cylinder 2. The slip boundaries were placed 25 diameters above and below the two cylinders, creating a blockage ratio of 2%.

The outer boundary was seeded in the exact same way as was done for a single cylinder. Figure 10 shows the mesh for $s = 4$. For $s \leqslant 4$, two mesh refinement boxes were used. An inner box with corners of $(-2, -1.5)$ and $(s + 2, 1.5)$ was used to keep a very fine mesh near the cylinders. An outer refinement box was used to ensure that the mesh did not grow uniformly to the outer boundary, but was refined nearer to the cylinders and in the wake region. The corners of this box were $(-8, -10)$ and $(s + 18, 10)$. The inner refinement box was not used

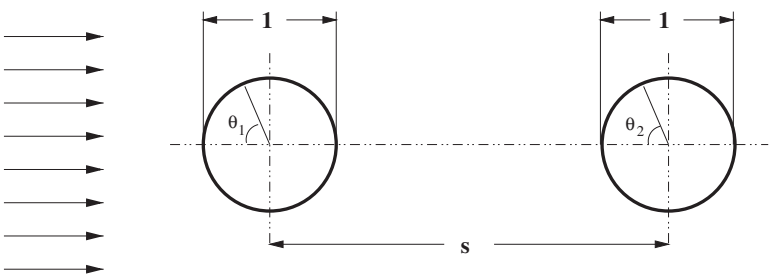

Figure 9. Two cylinders in a tandem arrangement.

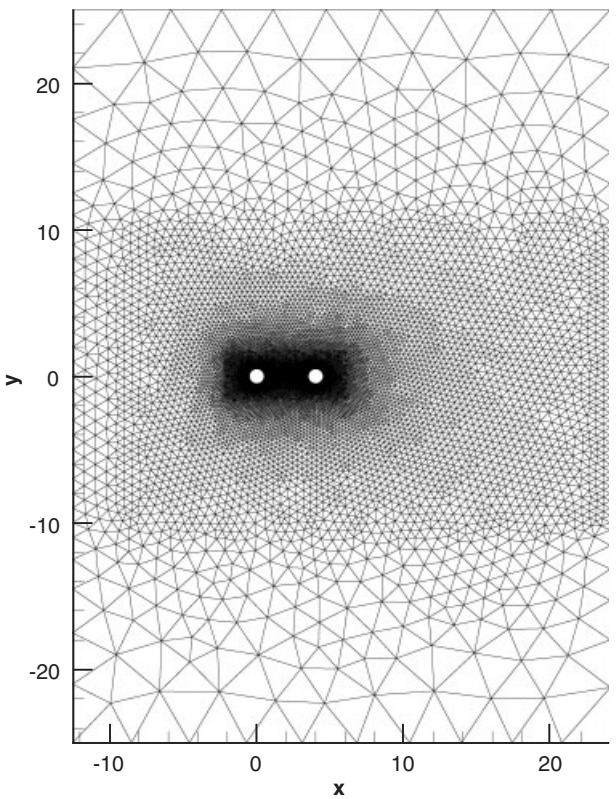

Figure 10. The computational mesh containing 23 892 cells for a flow over two tandem cylinders, $s = 4$, at $Re = 100$.

for $s \geqslant 6$ because the number of cells became too large for the available computing power. The mesh seeding on the inner refinement box was 0.1 diameters while that on the outer refinement box was 0.6 diameters.

5.2. Grid dependence study

Three different meshes (coarse, medium and fine) for $s = 4$ with grid spacings near the cylinder surface being $\pi/60 = 0.0523$, $\pi/90 = 0.0349$ and $\pi/120 = 0.0261$, respectively, are shown in Figure 11. The numerical errors associated with these meshes are estimated based on the lift coefficient C_l for the front cylinder with $240 \leqslant t \leqslant 280$ as follows (see Figure 12).

$$\text{error}(\%) \text{ on coarse mesh} = \frac{\sum_{t=t_{\min}}^{t=t_{\max}} \frac{|C_l^c - C_l^f|\,dt}{t_{\max} - t_{\min}}}{|C_l^f|_{\max}} \tag{24}$$

$$\text{error}(\%) \text{ on medium mesh} = \frac{\sum_{t=t_{\min}}^{t=t_{\max}} \frac{|C_l^m - C_l^f|\,dt}{t_{\max} - t_{\min}}}{|C_l^f|_{\max}} \tag{25}$$

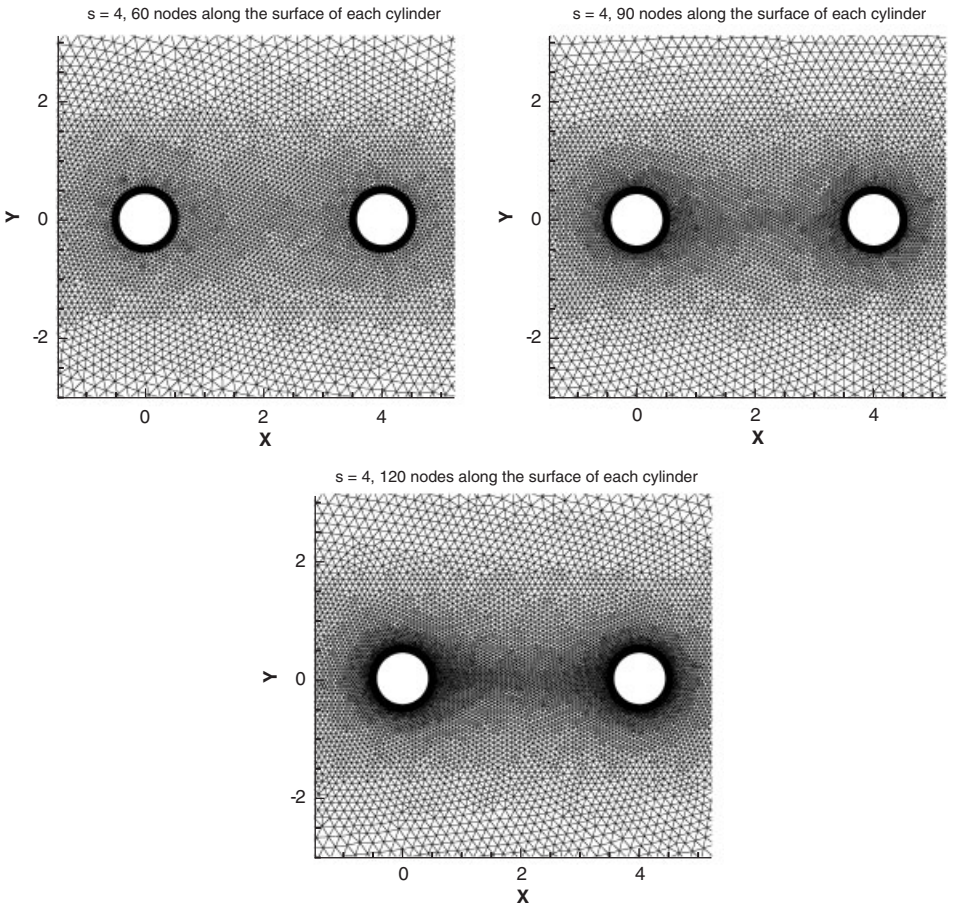

Figure 11. Three computational meshes for a flow over two tandem cylinders, $s = 4$.

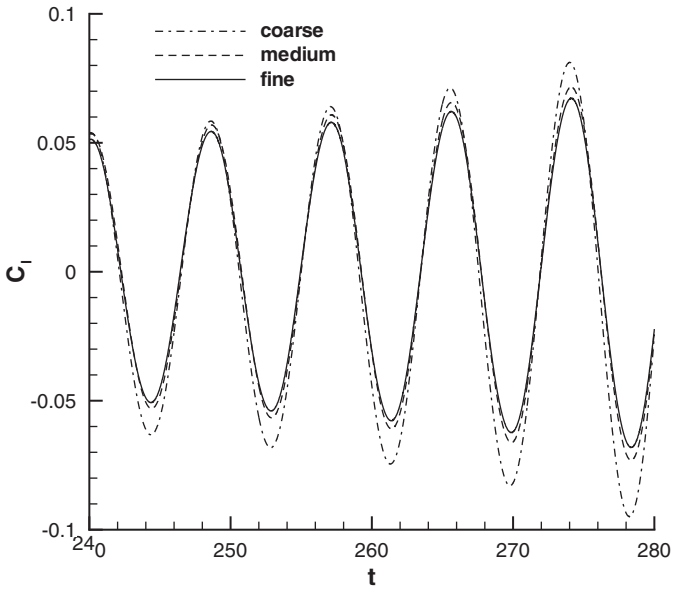

Figure 12. Distributions of lift coefficient C_l obtained on three different meshes for $240 \leqslant t \leqslant 280$ and $s = 4$.

where $|C_l^f|_{max}$ is the maximum $|C_l|$ on the fine mesh for $t_{min} \leqslant t \leqslant t_{max}$. The superscripts c, m and f in Equations (24) and (25) stand for coarse, medium and fine grids; $t_{min} = 260$, $t_{max} = 280$ and $dt = 0.005$ are used here, giving us 60 000 sample points used in the estimation of the numerical error based on the fine-grid solution. It is found that the errors associated with the coarse and medium grids are 13 and 3%, respectively. Results to be presented later are based on the medium grid.

5.3. *Global results—Strouhal number and lift and drag coefficients*

The Strouhal number in the present study was found to be the same for cylinder 1 and 2 for all cylinder spacings. Figure 14(a) compares the Strouhal numbers against the experimental data of Huhe-Aode *et al.* [6] and the numerical data of Li *et al.* [10]. This figure shows that the cylinder spacing has a large effect on the Strouhal number. The critical spacing is apparent, with a large and sudden jump in the Strouhal number as the critical spacing is passed.

Figure 13 shows snapshots of the instantaneous streamlines for $s = 2$ and 4. For $s = 2$, the wake off cylinder 1 is seen to reattach to cylinder 2. A symmetrical flow pattern is seen between the two cylinders. Long vortices are shed off cylinder 2, which explains the lower Strouhal number reported in Figure 14.

For $s = 4$, vortices are now also shed off of cylinder 1. These vortices move the reattachment point and energize the fluid so that it flows completely around cylinder 2. This effect is discussed further in Section 5.4. A significant amount of fluid that originally flowed below

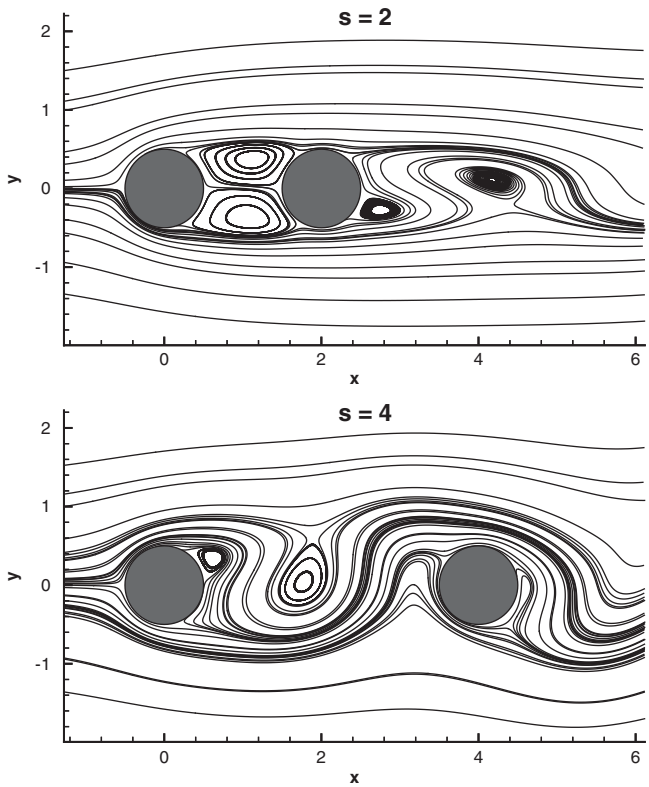

Figure 13. Snapshots of the instantaneous streamlines for $s = 2$ and 4.

cylinder 1 now flows over top of cylinder 2, which contributes to the large lift forces reported in Figure 14.

The data of Li *et al.* was interesting as they reported a different Strouhal number between the two cylinders. The data shown in Figure 14(a) were reported for cylinder 1. Their results for cylinder 2 are extremely different. No explanation for the difference was given.

The trends predicted by the different authors are similar, but large differences do exist. The current results indicate that the critical spacing is $3.75 \leqslant s_c \leqslant 4$, Huhe-Aode *et al.* measured that it is $4.5 \leqslant s_c \leqslant 5$, while Li *et al.* calculated it to be $3 \leqslant s_c \leqslant 4$.

As discussed in Section 1, neither the results of Huhe-Aode *et al.* nor those of Li *et al.* are deemed to be reliable. It was proven in this section that the experiment of Huhe-Aode *et al.* encountered three-dimensional effects because the cylinders were of insufficient aspect ratio. These three-dimensional effects were not understood at the time they conducted their experiment. The insufficient aspect ratio explained why the Strouhal number reported by Huhe-Aode *et al.* stayed at 0.141 for $s > s_c$.

It was also discussed that the results of Li *et al.* suffered from an insufficient domain, insufficient number of cells and large timesteps due to the lack of computational power available. Their results for a single cylinder did not agree well with recent accepted benchmark data.

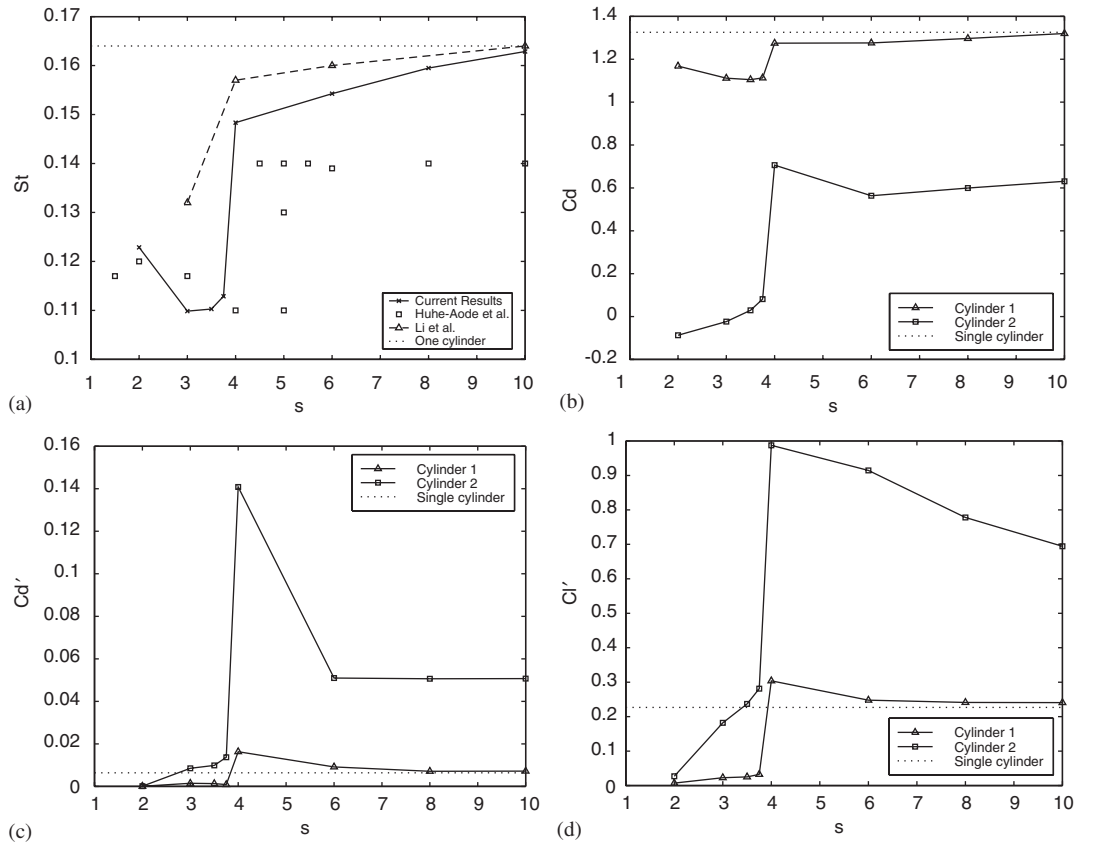

Figure 14. Strouhal number (a), mean drag coefficient (b), RMS drag coefficient (c), and RMS lift coefficient (d), vs cylinder spacing.

The results produced by the CUCFD program appear to be reasonable. The authors believe that since the CUCFD program was extremely accurate for flow over a single cylinder that it is also accurate for flow over two cylinders. It is hoped that future tests conducted by other researchers will verify the accuracy of the CUCFD results.

Figures 14(b)–14(d) show the mean drag, the fluctuating drag and the fluctuating lift respectively for the different cylinder spacings. The simulations were carried out up to $s = 10$. The critical spacing is very apparent in all of these figures. The mean drag of cylinder 2 is negative for small spacings, meaning that this cylinder is pushed forwards by the fluid. The drag slowly increases to small positive values and then jumps markedly at the critical spacing. The drag of cylinder 2 does not approach that of a single cylinder, even for large cylinder separations. The presence of cylinder 2 also reduces the drag of cylinder 1. This is because cylinder 2 increases the pressure in the separated wake behind cylinder 1, see Figure 17(a).

The fluctuating lift and drag coefficients follow similar trends as the spacing is increased. All fluctuations are small at $s = 2$. The fluctuations on cylinder 1 remain extremely low for

sub-critical spacings. These fluctuations become extreme as the spacing increases to $s = 4$. C_l' and C_d' are 4 and 22.4 times higher than that of a single cylinder, respectively, at this cylinder spacing. The fluctuations are slowly reduced as the cylinder spacing is increased beyond the critical spacing.

5.4. Separation points from the two cylinders

The location of separation and reattachment points on a body have a large effect on the forces acting upon it. The position of these points is also of great interest in explaining the surface pressure distributions, which are shown in Section 5.5. Figures 15 and 16 show close-up views of vorticity contours for $s = 2$ and 4. Separation and reattachment points occur at locations of zero vorticity and have been marked on these figures.

Cylinder 1 does not have any reattachment points as the oncoming flow is undisturbed. There are two separation points off of cylinder 1, one on the top and one on the bottom of the cylinder. For $s = 2$, the separation point was found to vary between 133 and 138° from the front stagnation point. For $s = 4$, the separation point moved further forward to between 118 and 125°.

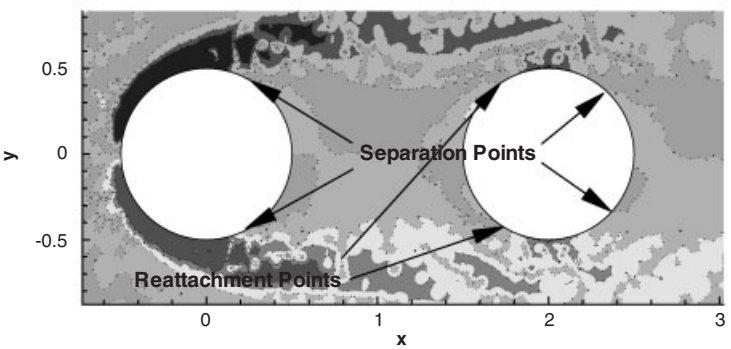

Figure 15. Instantaneous vorticity contours for $s = 2$.

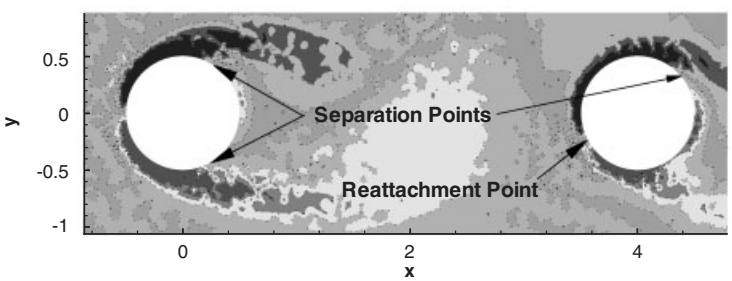

Figure 16. Instantaneous vorticity contours for $s = 4$.

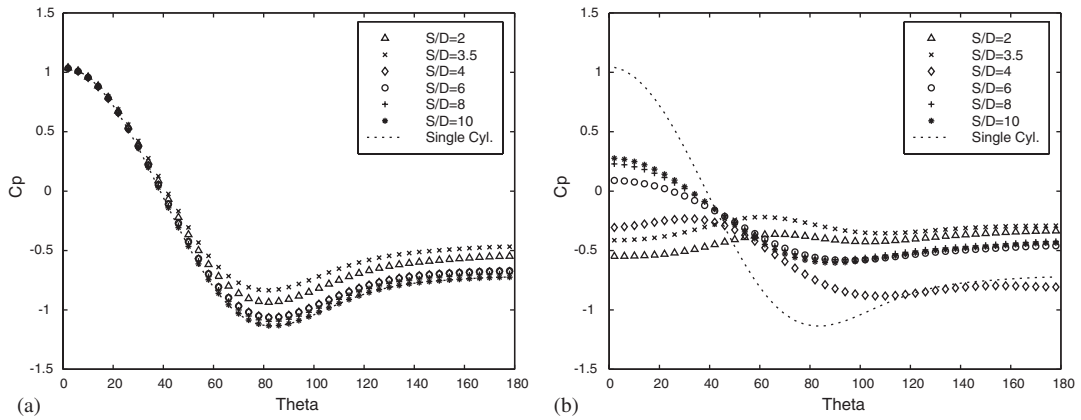

Figure 17. Mean surface pressure distribution for (a) upstream and (b) downstream cylinders for different cylinder spacings: (a) Cyl. 1, and (b) Cyl. 2.

The flow experienced by cylinder 2 changed markedly between $s=2$ and 4. For $s=2$, two separation and reattachment points exist. The reattachment points vary between 56 and 58° while the separation points vary between 133 and 138°. For $s=4$, there exists *only one reattachment and one separation point*. This was completely unexpected, but it can be seen by examining Figure 16. The reattachment and separation points flip from side to side during a flow cycle. The reattachment point varied between −41 and 41° while the separation point varied between 101 and 256°. The flow remains attached on both sides of the cylinder all because the pressure does not increase along the rear half of cylinder 2, see Figure 17(b).

5.5. *Mean and RMS surface pressure distributions*

The pressure lift and drag coefficients are a direct result of the pressure distribution on the surface of the cylinders. Pressure distributions were recorded for a single vortex shedding cycle.

Figures 17 and 18 show the mean and the RMS surface pressure distributions respectively. The mean pressure distribution around cylinder 1, Figure 17(a), is similar to that around a single cylinder for all cylinder spacings. The pressure at the rear of cylinder 1 is higher for low cylinder spacings than it is for larger spacings or for a single cylinder. This explains the reduced drag force on cylinder 1 for small cylinder spacings. Figure 17(b) shows that the mean pressure distribution around cylinder 2 never resembles that around a single cylinder.

The pressure fluctuations are very low around both cylinders when $s<s_c$. For cylinder 1, Figure 18(a), when the cylinder spacing is increased beyond s_c, the pressure fluctuations resemble those around a single cylinder. The pressure fluctuations tend towards that around a single circular cylinder as the cylinder spacing is increased. For cylinder 2, Figure 18(b), the pressure fluctuations do not resemble those around a single cylinder at any tested spacing.

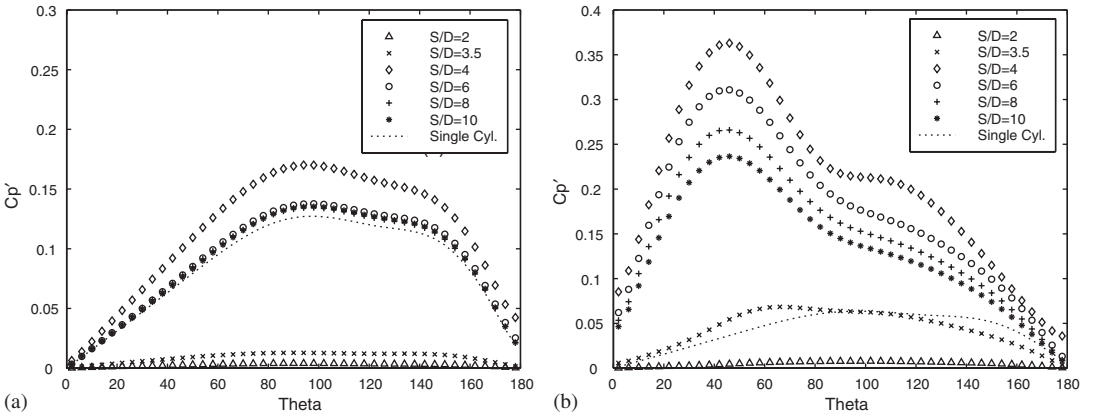

Figure 18. RMS surface pressure distribution for (a) upstream and (b) downstream cylinders for different cylinder spacings: (a) Cyl. 1, and (b) Cyl. 2.

The peak pressure fluctuations occur at $\theta \approx 45^\circ$ for $s > s_c$, which is near the reattachment points.

6. CONCLUSIONS

Benchmark test cases showed that the numerical discretization is accurate, especially for low Reynolds number flows.

The tests for a single cylinder for $Re = 100$ showed that the results agreed extremely well with recent benchmark tests. The accuracy of the results for these tests gave a great deal of confidence in the results from the CUCFD program.

Simulations were conducted for flow over two tandem cylinders at a Reynolds number of 100. The spacing between the cylinders was varied between 2 and 10 diameters. The mean and the RMS drag coefficients and the RMS lift coefficients were plotted as a function of the cylinder spacing. The existence of a critical spacing is very apparent, with a large jump in the fluctuating forces and the Strouhal number. The critical spacing was found to be between 3.75 and 4 cylinder diameters.

Two separation points existed on the upstream cylinder, one on the top and one on the bottom. For a cylinder separation of two diameters, two reattachment points and two separation points existed on the downstream cylinder, which was expected. Only one reattachment point and one separation point were found on the downstream cylinder at a cylinder spacing of four diameters. These points fluctuated between the top and the bottom sides of the cylinder.

The mean and the RMS surface pressure distributions showed that the surface pressures were greatly different between the upstream and the downstream cylinders. The pressure fluctuations were very low around both cylinders when the cylinder spacing was below the critical value. These fluctuations jumped markedly as the cylinder spacing was increased beyond critical spacings.

NOMENCLATURE

Greek letters—lowercase

α	weighting term used in discretization of diffusion discretization
α	relaxation factor
δ_{ij}	Kronecker delta, 1 if $i=j$, otherwise 0
μ	fluid viscosity
ρ	fluid density
ϕ	any arbitrary scalar

Greek letters—uppercase

Ω	volume (area for two-dimensional simulations)
Θ	angle from the front stagnation point

Latin letters—lowercase

a	coefficient for discretized pressure correction equation
m_f	mass flux through a face
m_f^*	mass flux through a face from the previous iteration
$\hat{\mathbf{n}}$	normalized face normal
nb	neighbouring cell
p	fluid pressure
p'	pressure correction
p^*	pressure from the previous iteration
$\mathbf{r}$	vector from the centroid of cell 0 to the centroid of cell 1
$\mathbf{r}_c$	vector from the midpoint between the centroids of cells 0 and 1 and the face midpoint
$\mathbf{r}_{0-f}$	vector from the centroid of cell 0 to the face midpoint
$\mathbf{r}_{1-f}$	vector from the centroid of cell 1 to the face midpoint
s	non-dimensionalized centre-to-centre distance between two tandem cylinders, S/D
s_c	critical non-dimensionalized centre-to-centre cylinder spacing
t	time
u, v	velocity components in the x- and y-direction, respectively
$\mathbf{v}$	fluid velocity vector
v'	velocity correction

Latin letters—uppercase

A	coefficient for momentum equation
D	cylinder diameter
B	source term for momentum equation
N	number of cells
P	identifier for current cell
R_m	mass imbalance for pressure-correction equation
S	surface area (length for two-dimensional simulations)
U	flow velocity

$V0$	vertex 0 of face
$V1$	vertex 1 of face

Subscripts

bnd	value at the boundary
d	drag
dp	pressure drag
dv	viscous drag
f	value at face midpoint
i	direction 'i'
i	instantaneous quantity
j	direction 'j'
l	lift
lp	pressure lift
lv	viscous lift
mean	mean value for fluctuating quantities
nb	neighbouring cell
p	pressure
pb	back pressure, pressure at the rear of the cylinder
ps	stagnation pressure, pressure at the front stagnation point
s	separation point
P	current cell
0	applies at cell '0'
1	applies at cell '1'
∞	free-stream value

ACKNOWLEDGEMENTS

The first two authors are grateful to the Natural Sciences and Engineering Research Council of Canada (NSERC) for the financial support of this work. The first author is grateful for the support and guidance he received during his one-year visit to the Thermo and Fluid Dynamics Department at Chalmers University of Technology, Sweden.

REFERENCES

1. Zdravkovich MM. *Flow Around Circular Cylinders—Volume* 1: *Fundamentals*. Oxford University Press: Oxford, 1997.
2. Ohya YO, Okajima A, Hayashi M. Wake Interference and Vortex Shedding. *Aerodynamics and Compressible Flow*, vol. 8. Gulf Publishing Company: Houston, TX, 1989; 322–389.
3. Igarashi T. Characteristics of the flow around two circular cylinders of different diameters arranged in tandem. *Bulletin of the JSME* 1981; **24**:323–331.
4. Zdravkovich MM. Flow-induced oscillations of two interfering circular cylinders. *Journal of Sound and Vibration* 1985; **101**:511–521.
5. Ljungkrona L, Norberg C, Sunden B. Free-stream turbulence and tube spacing effect on surface pressure fluctuations for two tubes in an in-line arrangement. *Journal of Fluids and Structures* 1991; **5**:701–727.
6. Huhe-Aode, Tatsuno M, Taneda S. Visual studies on wake structure behind two cylinders in tandem arrangement. *Reports of Research Institute for Applied Mechanics*, vol. XXXII(99), 1985.
7. Tanida Y, Okajima A, Watanabe Y. Stability of circular cylinder oscillating in uniform flow or in a wake. *Journal of Fluid Mechanics* 1973; **61**:769–784.

8. Norberg C. An experimental investigation of the flow around a circular cylinder: influence of aspect ratio. *Journal of Fluids Mechanics* 1994; **258**:287–316.
9. Williamson CHK. Oblique and parallel modes of vortex shedding in the wake of a circular cylinder at low-Reynolds numbers. *Journal of Fluid Mechanics* 1989; **206**:579–627.
10. Li J, Chambarel A, Donneaud M, Martin R. Numerical study of laminar flow past one and two circular cylinders. *Computers and Fluids* 1991; **19**:155–170.
11. Mittal S, Kumar V, Raghuvanshi A. Unsteady incompressible flows past two cylinders in tandem and staggered arrangements. *International Journal for Numerical Methods in Fluids* 1997; **25**:1315–1344.
12. Slaouti A, Stansby PK. Flow around two circular cylinders by the random vortex method. *Journal of Fluids and Structures* 1992; **6**:641–670.
13. Meneghini JR, Saltara F, Siqueira CLR, Ferrari Jr JA. Numerical simulation of flow interference between two circular cylinders in tandem and side-by-side arrangements. *Journal of Fluids and Structures* 2001; **15**:327–350.
14. Karamete K. Available on the Internet: http://scorec.rpi.edu/∼kaan/
15. Niceno B. Available on Internet: http://www-dinma.univ.trieste.it/∼nirftc/research/easymesh/easymesh.html
16. Rhie CM, Chow WL. A numerical study of the turbulent flow past an isolated airfoil with trailing edge separation. *AIAA Journal* 1983; **21**:1525–1532.
17. Caretto LS, Gosman AD, Patankar SV, Spalding DB. Two calculation procedures for steady, three-dimensional flows with recirculation. *Proceedings of the Third Conference on Numerical Methods in Fluid Dynamics*, Paris, 1972.
18. Trim D. *Calculus*. Prentice-Hall Canada Inc., 1993.
19. Zwart P. The integrated space–time finite volume method. *Ph.D. Thesis*, University of Waterloo, Waterloo, Ontario, Canada, 1999.
20. Sharman B. Numerical predictions of low Reynolds number flow over two tandem circular cylinders. *Master's Thesis*, University of Waterloo, Waterloo, Ontario, Canada, 2002.
21. Ferziger JH, Peric M. *Computational Methods for Fluid Dynamics* (2nd edn). Springer: Berlin, 1999.
22. Barrett R, Berry M, Chan TF, Demmal J, Donato J, Dongarra J, Eijkhout V, Pozo R, Romine C, Van der Vorst H. *Templates for the Solution of Linear Systems: Building Blocks for Iterative Methods* (2nd edn). SIAM: Philadelphia, PA, 1994.
23. Le H, Moin P. Direct numerical simulation of turbulent flow over a backward-facing step. *Report No. TF-58*, Department of Mechanical Engineering, Stanford University, 1994.
24. Emvin P. The full multigrid method applied to turbulent flow in ventilated enclosures using structured and unstructured grids. *Ph.D Thesis*, Chalmers University of Technology, Göteborg, 1997.
25. Norberg C. Fluctuating lift on a circular cylinder: review and new measurements. *Journal of Fluids and Structures* 2003; **17**:57–96.
26. Posdziech O, Grundmann R. *Technical report*, TU Dresden, Germany.
27. Park J, Kwon K, Choi H. Numerical solutions of flow past a circular cylinder at Reynolds numbers up to 160. *KSME International Journal* 1998; **12**(6):1200–1205.

